

Plane waves in periodic, quadratically nonlinear slab waveguides: stability and exact Fourier structure

Joel F. Corney and Ole Bang

*Informatics and Mathematical Modelling, Technical University of Denmark,
DK-2800 Kongens Lyngby, Denmark*

Received May 16, 2001; revised manuscript received August 20, 2001

We consider the propagation of broad optical beams through slab waveguides with a purely quadratic nonlinearity and containing linear and nonlinear long-period quasi-phase-matching gratings. An exact Floquet analysis of the periodic, plane-wave solution shows that the periodicity can drastically alter the growth rate of the modulational instability but that it never completely removes the instability. The results are confirmed by direct numerical simulation as well as through a simpler, approximate theory for the averaged fields that accurately predicts the low-frequency part of the gain spectrum. © 2002 Optical Society of America

OCIS codes: 190.5530, 230.4320, 190.4410, 190.5940.

1. INTRODUCTION

Optical materials with $\chi^{(2)}$ nonlinearity offer many advantages as candidates for all-optical processing applications. For example, they offer a fast and strong nonlinear response, and through cascading $\chi^{(2)}:\chi^{(2)}$ processes¹ they can support stable localized solitary-wave solutions in more than one dimension,²⁻⁶ in contrast with systems that have only a cubic nonlinear response. Experimental studies have confirmed the existence of one-⁷ and two-dimensional⁸ spatial and spatiotemporal⁹ quadratic solitons and have demonstrated that they act as dynamically reconfigurable guiding structures,¹⁰ with switching behavior controllable through phase-¹¹ and intensity-dependent¹² effects. Even though special dark-vortex solitons have been generated in quadratic media,¹³ coherent dark solitons are generally unstable in homogeneous materials with only quadratic nonlinearity because of modulational instability (MI) in the background plane wave.

Like solitons, MI occurs as the result of an interplay between nonlinear and dispersive or diffractive effects. In nonlinear optics, it appears as a transverse instability that breaks up a broad optical beam,¹⁴ thereby acting as a precursor for the formation of stable bright spatial solitons, as has been confirmed experimentally.¹⁵ Conversely, the stable propagation of dark solitons relies on the stability of the constant-intensity background and thus requires the absence of MI. The mismatch⁹ and intensity¹⁶ dependence of the instability period has been investigated experimentally, as has the intensity and frequency dependence of the gain.¹⁷

In all $\chi^{(2)}$ materials there is of course an inherent cubic (Kerr) nonlinearity. The combined nonlinearities lead to novel effects, such as the existence of bright solitons in an intrinsically defocusing cubic medium.¹⁸ Also, if the defocusing cubic nonlinearity is sufficiently strong, it may eliminate MI.¹⁹ Unfortunately, the cubic nonlinearity in conventional $\chi^{(2)}$ materials is usually fo-

cus and thus of the wrong type for these effects to occur.

However, a cubic nonlinearity of a different kind may be induced through long-period variations in the linear or nonlinear susceptibilities. Such periodicities are used for quasi-phase matching (QPM), which compensates for the material mismatch between the fundamental and the second-harmonic (SH) modes. The lowest-order effect of QPM is to induce an effectively phase-matched quadratic nonlinearity in the equations for the averaged fields. To first order, the non-phase-matched oscillatory components of the fields induce cubic nonlinearities²⁰⁻²³ in the same manner as the non-phase-matched interactions do in the cascading limit.²³ For certain materials and etching techniques, altering the nonlinear susceptibility also induces a change in the linear susceptibility. The action of such a simultaneous linear grating can be to reduce the effective quadratic nonlinearity,²⁴⁻²⁸ making the effective nonlinearity more cubic, as in the cascading limit.

In this paper we investigate the effects of such periodicities on the MI properties of beams in $\chi^{(2)}$ materials, considerably extending the initial results presented in Ref. 29. We provide a comprehensive and comparative treatment of the different approaches (exact and approximate) and use a variety of particular cases to illustrate general properties. In Section 2 we introduce the system studied in the rest of the paper. In analyzing this system, we first (Section 3) seek modulationally stable dark solitons in an approximate averaged system. Previous studies^{21,22} confirmed the accuracy of the averaged theory in describing the average properties of solitons and cw switching,^{30,31} showing that this intrinsically quadratically nonlinear system behaves as though it were governed by cubic as well as quadratic nonlinearities. The theory also describes space-varying behavior but with a lower accuracy. We discover that the cubic terms that result from particular gratings can be large enough and of the correct sign to prevent MI.

In the second part of this paper we compare the stability predictions of the averaged theory with those of exact calculations. The exact methods involve finding the exact periodic plane-wave solutions in the full (nonaveraged) system, with the higher harmonics included to all orders (Section 4). We apply a Floquet analysis to these periodic solutions to determine the growth rate of linear perturbations (Section 5), which can now be directly probed in experiments.¹⁷ Additionally, we directly simulate the periodic-field equations (Section 6), using for initial conditions the averaged solutions seeded with noise.

According to the exact calculations, the periodicities can drastically alter the MI gain spectrum, but they do not entirely remove the inherent instability. We find that in the regime of efficient QPM the MI gain spectrum contains two distinct and well-separated features with fundamentally different physical origins (see Subsection 5.B below). The low-frequency part of the gain is accurately predicted by the averaged theory and disappears for certain grating modulations. The high-frequency part of the spectrum is related to the inherent gain of the non-phase-matched material (i.e., with no gratings) and appears to be unavoidable. However, because they are consistently small, the high-frequency peaks can be ignored under a less stringent definition of experimental stability (see Subsection 5.D). This gives the possibility of stable plane waves as predicted by the averaged theory.

2. SYSTEM

We consider a cw beam (carrier frequency ω) interacting with its SH, both propagating in a lossless one-dimensional slab waveguide under conditions for type I SH generation. Both the linear and the quadratic nonlinear susceptibilities are periodic along the Z direction of propagation but are constant along the transverse X direction. We assume a weak modulation of the refractive index [$\Delta n_j(Z)/\bar{n}_j \ll 1$, where $n_j(Z) = \bar{n}_j + \Delta n_j(Z)$ and j refers to the frequency $j\omega$]. We consider gratings for forward QPM only. The grating period is then much longer than the optical period, in which case Bragg reflections can be neglected. The evolution of the slowly varying beam envelopes is then described by³²

$$\begin{aligned} i\partial_z E_1 + 1/2\partial_x^2 E_1 + \alpha_1 E_1 + \chi E_1^* E_2 \exp(i\beta Z) &= 0, \\ i\partial_z E_2 + 1/4\partial_x^2 E_2 + 2\alpha_2 E_2 + \chi E_1^2 \exp(-i\beta Z) &= 0, \end{aligned} \quad (1)$$

where $E_1 = E_1(X, Z)$ and $E_2 = E_2(X, Z)$ are the envelope functions of the fundamental and the SH, respectively. The coordinates X and Z are in units of input beam width X_0 and diffraction length $L_d = k_1 X_0^2$, respectively. The parameter $\beta = \Delta k L_d$ is proportional to the mismatch $\Delta k = k_2 - 2k_1$, where $k_j = j\omega\bar{n}_j/c$ is the average wave number. Thus β is positive for normal dispersion and negative for anomalous dispersion. The normalized refractive-index grating is $\alpha_j(Z) = L_d \omega \Delta n_j(Z)/c$, and the normalized nonlinear grating is $\chi(Z) = L_d \omega d_{\text{eff}}(Z)/(\bar{n}_1 c)$, where $d_{\text{eff}} = \chi^{(2)}/2$ is given in MKS units. The model [Eqs. (1)] describes both temporal and spatial solitons.^{33,34} Throughout this paper we focus on

first-order QPM, using conventional square gratings with a 50% duty cycle, as shown in Fig. 1.

To consider plane-wave solutions with longitudinal wave-number offset Λ and transverse wave number Ω , we introduce the new variables $w(x, z) = E_1(X, Z) \times \exp(i\Theta)$, $v(x, z) = E_2(X, Z) \exp(2i\Theta + i\beta Z)$, $x = \sqrt{\eta}(X + \Omega Z)$, and $z = \eta Z$, where $\Theta(Z) = \Omega X - \Lambda Z - \int \alpha_1(Z) dZ$ and where $\eta = |\Lambda + 1/2\Omega^2|$ for $\Lambda \neq -1/2\Omega^2$ and $\eta = 1$ otherwise. We have also introduced a residual effective mismatch $\tilde{\beta} = \beta - k_g$, where k_g is the spatial frequency of the gratings. This gives the rescaled equations

$$i\partial_z w + 1/2\partial_x^2 w - rw + \chi' w^* v \exp(i\kappa z) = 0,$$

$$i\partial_z v + 1/4\partial_x^2 v - \sigma v + \alpha' v + \chi' w^2 \exp(-i\kappa z) = 0, \quad (2)$$

where $r = \text{sgn}(\Lambda + 1/2\Omega^2)$, $\kappa = k_g/\eta$, and $\sigma = 2r - \tilde{\beta}'$ for $\tilde{\beta}' = \tilde{\beta}/\eta$. Note that $r = 0$ when $\Lambda = -1/2\Omega^2$. This scaling by η may be absorbed into the original normalization [Eqs. (1)] through a redefinition of X_0 (and hence of L_d) to be something other than the true beam width (diffraction length). We choose to retain η explicitly, however, to show the connection with the standard normalization.

To find solutions in this periodic system, we Fourier expand the rescaled gratings, $\alpha'(z) = 2[\alpha_2(Z) - \alpha_1(Z)]/\eta$ and $\chi'(z) = \chi(Z)/\eta$:

$$\alpha' = a' \sum_n g_n \exp(in\kappa z),$$

$$\chi' = d'_0 + d' \sum_n g_n \exp(in\kappa z), \quad (3)$$

where $a' = 2(a_2 - a_1)/\eta$ and where $g_n = 2s/(i\pi n)$ for n odd and $g_n = 0$ for n even. We include $s = \text{sgn}(\kappa)$ in the Fourier expansions to ensure that the expansions give the same physical grating form for both signs of κ . Plane waves in the systems of Eqs. (1) and (2) have an intensity that is constant in the transverse direction but periodic in Z , driven by the periodic variation of the susceptibilities. Thus they have the same spatial frequency κ as the gratings, and we expand them in Fourier series also:

$$w = \sum_n w_n(x, z) \exp(in\kappa z),$$

$$v = \sum_n v_n(x, z) \exp(in\kappa z). \quad (4)$$

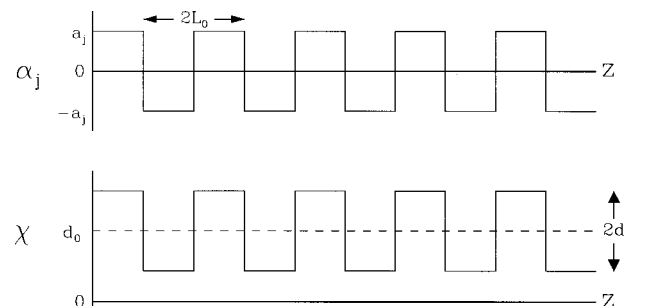


Fig. 1. Periodic linear and quadratically nonlinear gratings, $\alpha_j(Z)$ and $\chi(Z)$, with period $2L_0 = 2\pi/|k_g|$.

An accurate treatment of the problem requires that all Fourier components (up to some cutoff) be included. This we do in Section 4 below. However, first we present an approximate theory for the dc components $(\bar{w}, \bar{v}) = (w_0, v_0)$, which suffices for many calculations.

3. AVERAGED-FIELD THEORY

A. Plane-Wave Solutions

Three physical length scales are in play: diffraction length L_d , coherence length L_c , and grating domain length L_0 . In our rescaled units, $L_d = \eta$, $L_c = \eta\pi/|\beta| \equiv \pi/|\beta'|$, and $L_0 = \pi/|\kappa|$. We assume a typical QPM grating with a domain length that is much shorter than the diffraction length and use perturbation theory²⁰ with the small parameter $\epsilon = L_0/L_d \ll 1$. We insert the Fourier expansions (3) and (4) into the dynamic equations and assume the harmonics $w_{n \neq 0}$ and $v_{n \neq 0}$ to be of order ϵ . Furthermore, efficient phase matching is assumed, with the domain length being close to the coherence length, $L_0 \approx L_c$, so the residual mismatch is small, $|\beta'| \ll |\kappa|$. To first order (ϵ^1), this gives the harmonics

$$\begin{aligned} w_{n \neq 0} &= \frac{(d'g_{n-1} + d'_0\delta_{n,1})w_0^*v_0}{n\kappa}, \\ v_{n \neq 0} &= \frac{a'g_nv_0 + (d'g_{n+1} + d'_0\delta_{n,-1})w_0^2}{n\kappa}, \end{aligned} \quad (5)$$

where $\delta_{n,m}$ is Kronecker's delta function and where we have assumed that the coefficients $w_n(x, z)$ and $v_n(x, z)$ vary slowly in z compared with $\exp(i\kappa z)$. Using these solutions, we obtain to first order the averaged equations for the dc components $(\bar{w}, \bar{v}) = (w_0, v_0)$:

$$\begin{aligned} i\partial_z\bar{w} + 1/2\partial_x^2\bar{w} - r\bar{w} + \rho\bar{w}^*\bar{v} + \gamma(|\bar{v}|^2 - |\bar{w}|^2)\bar{w} &= 0, \\ i\partial_z\bar{v} + 1/4\partial_x^2\bar{v} - \sigma\bar{v} + \rho^*\bar{w}^2 + 2\gamma|\bar{w}|^2\bar{v} &= 0. \end{aligned} \quad (6)$$

Equations (6) also describe m th-order QPM (where $\tilde{\beta} = \beta - mk_g$ is ideally zero) and any other type of long-period grating. Incorporating time or the spatial y coordinate is also straightforward. The effective quadratic (ρ) and induced cubic (γ) nonlinearities are simply given by sums over the Fourier coefficients²⁰ and for the square grating [Eqs. (3)] are $\rho = i2s[d' - d'_0a'/\kappa]/\pi$ and $\gamma = [d_0'^2 + d'^2(1 - 8/\pi^2)]/\kappa$.

From Eqs. (6) follows the important result that cubic nonlinearities are induced by the nonlinear QPM gratings. This cubic nonlinearity has the form of asymmetric self- and cross-phase modulations and is a result of non-phase-matched coupling between the wave at the main spatial frequency κ and its higher harmonics. It is thus of a fundamentally different nature from the material Kerr nonlinearity, a fact that is reflected in the the cross-phase modulation's being absent for the SH.

The induced cubic nonlinearity depends only on the nonlinear grating and may lead to either a focusing or a defocusing effect, depending on the relative intensity of the fields and the sign of the phase mismatch β' , because $\text{sgn}(\kappa) = \text{sgn}(\beta')$. The effective $\chi^{(2)}$ nonlinearity receives a contribution from the linear grating, which can either

reinforce or undermine the contribution from the nonlinear grating, depending on the physical situation.^{26,27}

Any plane wave will correspond to a stationary solution (\bar{w}_s, \bar{v}_s) of Eqs. (6), obtained by setting the derivatives to zero. By using a gauge transformation we make \bar{w}_s real and positive. The solutions are then $\bar{w}_s = \sqrt{y}/|\rho|$ and $\bar{v}_s = y/(\sigma\rho - 2\tilde{\gamma}y\rho)$, where y is a positive, real number that satisfies

$$\begin{aligned} 0 &= 4\tilde{\gamma}^3y^3 + \tilde{\gamma}[1 + 4\tilde{\gamma}(r - \sigma)]y^2 \\ &\quad + \sigma(\tilde{\gamma}\sigma - 4r\tilde{\gamma} - 1)y + r\sigma^2. \end{aligned} \quad (7)$$

For given r , $\tilde{\gamma}$, and σ there can thus be as many as three solutions. The relative strength of the cubic nonlinearity is given by the parameter $\tilde{\gamma} = \gamma/|\rho|^2$, which depends only on the material grating parameters κ , a'/β' , and d'_0/d' . Note that the residual-mismatch term σ equals $2r$ for perfect phase matching.

The solutions in parameter space $(\tilde{\gamma}, \sigma)$ are illustrated by the intensity ratio $R = \bar{v}_s^2/\bar{w}_s^2$ in Fig. 2 for $r = -1$. The figure shows that there are four extended branches of solution, which exist in three quadrants; the fourth quadrant is devoid of any solution. We label the pervasive branch G and the upper branch in the negative quadrant U2. The boundaries of G and U2 lie along the $\tilde{\gamma}$ and σ axes and are located where the ratio R tends to infinity. The positive quadrant contains additional paired upper (U1) and lower (L1) branches, which exist only away from the axes, their boundary given by

$$\sigma(\tilde{\gamma}) = [5 + 16\tilde{\gamma} + 3(\sqrt[3]{f_-} + \sqrt[3]{f_+})]/(8\tilde{\gamma}), \quad (8)$$

where $f_{\pm} = -1 + 80\tilde{\gamma} + 128\tilde{\gamma}^2 \pm 16[\tilde{\gamma}(-1 + 4\tilde{\gamma})^3]^{1/2}$. Note that, for $\tilde{\gamma} < 1/4$, we must take the roots of f_{\pm} that give the largest real σ . Equation (8) tells us that U1 and L1 exist only for $\tilde{\gamma} > 0$ and $\sigma > 2$.

Note that the $r = -1$ solutions can be transformed into the $r = 1$ solutions by the replacements $\bar{v}_s \rightarrow -\bar{v}_s$, $\sigma \rightarrow -\sigma$, and $\tilde{\gamma} \rightarrow -\tilde{\gamma}$. However, the MI properties differ. In addition to the solutions in Fig. 2, there are also a trivial solution $(\bar{w}_s, \bar{v}_s) = (0, 0)$ and a degenerate solution $(\bar{w}_s, \bar{v}_s) = (0, \text{arbitrary})$ that exist for $\sigma = 0$. However, the degenerate solution does not correspond to any dark-soliton solution, even though it is sometimes stable, as there is no nonlinearity in the equation for \bar{v}_s when $\bar{w}_s = 0$.

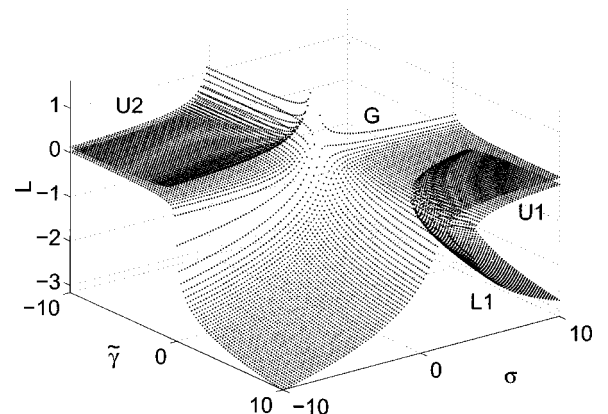


Fig. 2. Ratio of intensities $L = \log(\bar{v}_s^2/\bar{w}_s^2)$ for plane-wave solutions, as a function of $\tilde{\gamma}$ and σ , for $r = -1$.

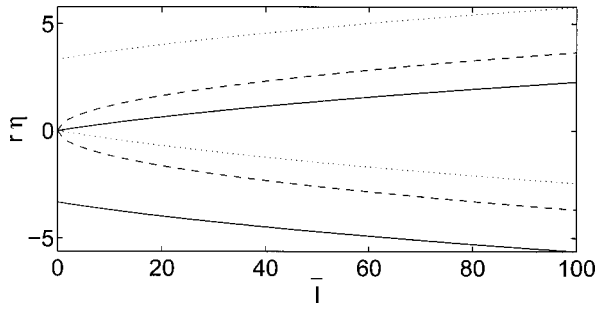


Fig. 3. Parameter $r\eta$ versus averaged intensity \bar{I} for $\tilde{\beta} = -10$ (solid curves), $\tilde{\beta} = 0$ (dashed curves), and $\tilde{\beta} = 10$ (dotted curves), with $d_0 = 0$, $d = 1$, and $k_g = 100$.

To relate solutions (7) to a specific physical situation requires that the plane-wave variables r and η , and hence Ω and Λ , be known, because r specifies the solutions and η is scaled into the normalized units and grating parameters. Now Ω is determined by the angle of the plane wave to the Z axis and is zero at normal incidence. In contrast, Λ is not directly accessible in experiments; it depends on the intensities of the fundamental and the SH and must be determined through a nonlinear dispersion relation. In the limit $\tilde{\gamma} \ll 1$, the cubic terms can be ignored, yielding $r = [\tilde{\beta}' \pm (\tilde{\beta}'^2 + 12\bar{I}|\rho|^2)^{1/2}]/6$, where $\bar{I} = |\bar{w}|^2 + |\bar{v}|^2$ is the averaged intensity. In unscaled units, $\eta r = [\beta \pm (\beta^2 + 12\bar{I}|\rho_{UN}|^2)^{1/2}]/6$, where $\rho_{UN} = \eta\rho$ now has no dependence on η . Which root of the radical is taken depends on the relative sizes of the two field intensities. When cubic terms need to be included, a simple analytic expression for r on $r\eta$ is not possible, and the calculation must be done numerically. For example, Fig. 3 illustrates the dependence of $r\eta$ on \bar{I} and on $\tilde{\beta}$ for a symmetric nonlinear grating. The two branches of the solution are distinguished by different ratios of the fundamental to the SH. Where a choice of η is required in Sections 4–6 below, we simply take $\eta = 1$, which can be satisfied by an appropriate choice of intensity \bar{I} and input width X_0 .

B. Modulation Instability

Following standard MI analysis,^{19,35,36} we assume that the plane-wave solutions \bar{w}_s and \bar{v}_s of Eqs. (6) are perturbed by small modulations:

$$\begin{aligned} \bar{w}(z) &= \bar{w}_s + \bar{\delta}_1(z)\exp(-i\nu x) + \bar{\delta}_2^*(z)\exp(i\nu x), \\ \bar{v}(z) &= \bar{v}_s + \bar{\delta}_3(z)\exp(-i\nu x) + \bar{\delta}_4^*(z)\exp(i\nu x), \end{aligned} \quad (9)$$

where $*$ denotes a complex conjugate. The linear growth is governed by $\partial_z \bar{\Delta}(z) = \bar{M}\bar{\Delta}(z)$, where

$$\bar{\Delta} = \begin{pmatrix} \bar{\delta}_1 \\ \bar{\delta}_2 \\ \bar{\delta}_3 \\ \bar{\delta}_4 \end{pmatrix}, \quad \bar{M} = i \begin{bmatrix} a & b & c & d \\ -b & -a & -d & -c \\ 2c & 2d & g & 0 \\ -2d & -2c & 0 & -g \end{bmatrix}, \quad (10)$$

with $a = -\nu^2/2 - r + \gamma(|v_s|^2 - 2w_s^2)$, $b = \rho v_s - \gamma w_s^2$, $c = \rho w_s + \gamma v_s w_s$, $d = \gamma v_s w_s$, and $g = -\nu^2/4 - \sigma + 2\gamma w_s^2$. For MI to be absent, all the eigenvalues λ_i of

\bar{M} must be imaginary. In practice, we calculate the gain at a finite number of values of ν , to a maximum of $\nu = 50$.

For $r = 1$ and $r = 0$, stability analysis shows that all nondegenerate and nontrivial solutions are unstable. For the $r = -1$ solutions, however, the L1 branch of solutions is stable. Figure 4 shows the region of stability, which differs significantly from that found in Ref. 19 because of the asymmetric nature of the induced cubic nonlinearity in Eqs. (6). The solid curve in Fig. 4 is the boundary of L1. Now, on this branch, $\tilde{\gamma}$ and σ cannot both be small, suggesting that there are two possible ways to achieve stability. One is to have a relatively large cubic nonlinearity $\tilde{\gamma}$; the other, a large mismatch σ . Increasing the size of $\tilde{\gamma}$ basically entails decreasing ρ , the size of the effective quadratic nonlinearity, if the perturbation theory is to remain valid. However, in most applications a large effective $\chi^{(2)}$ is desirable. The other possible route to stability is to increase σ , i.e., to increase

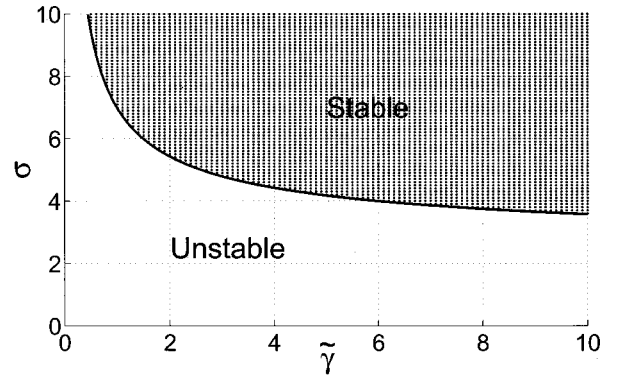


Fig. 4. Regions of stability and instability for the $r = -1$ solutions.

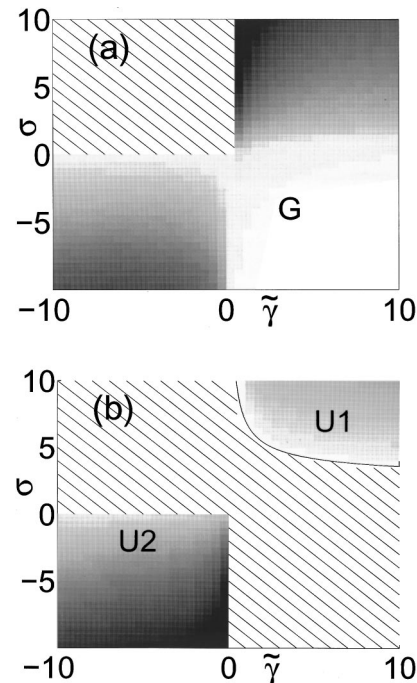


Fig. 5. Maximum gain of unstable branches (a) G and (b) U1 and U2 of the $r = -1$ solutions (black is the largest gain). Hatching indicates the absence of a solution.

$-\tilde{\beta}' = -\tilde{\beta}/\eta$. However, this large residual mismatch may also invalidate the perturbation theory. (η cannot be reduced, because this would decrease $\tilde{\gamma}$, thereby moving the solution further from the stable region.) Thus whether this region of stability truly exists must be determined by more-exact methods.

Figure 5 plots the maximum gain of the unstable branches G, U1, and U2. It shows several regions where the gain is small, namely, close to the existence boundaries of the solutions G, U1, and U2 and also for G when $\tilde{\gamma} \gg 1$ and $\sigma \ll -1$. Most of these almost-stable regions coincide with either \bar{w}_s or \bar{v}_s becoming small. For example, near $\sigma = 0$, solutions G and U2 approach the degenerate solution ($\bar{w}_s = 0$) for $\tilde{\gamma} < 1/4$; when $\tilde{\gamma} \gg 1$ and $\sigma \ll -1$, the SH in G approaches zero. In these cases, the averaged equations effectively become either linear or a nonlinear Schrödinger equation. The exception is branch U1: Its gain becomes small in the region near where it meets the stable (L1) branch, as expected. Now, some of these solutions have such low gain that for experimental purposes they will appear to be stable. Figure 5 tells us that such experimentally stable solutions lie in diverse regions in parameter space and thus may be more accessible than the mathematically stable solutions.

We show in Fig. 6 the gain profiles for $\tilde{\gamma} = 0$ of the G solution, which are found when the induced cubic terms are ignored, i.e., when the first-order terms are not taken into account in the perturbation theory. The same gain curves appear when there is no grating, with effective mismatch $\tilde{\beta}$ replaced by (much larger) inherent mismatch β in the expression for σ , which gives a larger $|\sigma|$. Thus, to zeroth order, the effect of the periodic grating is to increase and broaden the gain, because a much smaller $|\sigma|$ is achieved than in the non-phase-matched case without a grating. However, the more accurate first-order theory involves a further adjustment to the spectrum, with the inclusion of the cubic terms (such that $\tilde{\gamma} \neq 0$). The cubic terms may decrease the maximum gain, perhaps even to zero for particular gratings.

C. Cubic Solutions: $\rho = 0$

For some combinations of linear and nonlinear gratings, the cubic nonlinearity may dominate the quadratic. In the extreme case, the effective quadratic nonlinearity is zero ($\rho = 0$), caused by the linear grating (multiplied by the strength of the dc nonlinearity) canceling the contribution of the nonlinear grating, which can occur for realistic physical parameters. The averaged-field equations reduce to two NLS equations, which support the stable dark solitons (for $r = -1$):

$$\bar{w} = \tanh(x)/\sqrt{\gamma}, \quad \bar{v} = 0 (\gamma > 0), \quad (11)$$

$$\bar{w} = \tanh(x)/\sqrt{|4\gamma|}, \quad \bar{v} = \pm\sqrt{5/|4\gamma|}\tanh(x) (\gamma < 0), \quad (12)$$

where $\sigma = -1/2$ in the second solution [Eq. (12)]. In the absence of the parametric term, the two averaged fields are coupled only by phase-independent XPM terms, which is why these solutions do not possess the natural $\chi^{(2)}$ phase relation: In the first solution [Eq. (11)], σ is arbitrary, and the second solution [Eq. (12)] exists only for a particular, nonzero value of the residual mismatch $\tilde{\beta}' = -3/2$.

The plane-wave backgrounds of the solitons [Eqs. (11) and (12)] form part of a larger set of plane-wave solutions that exist in the absence of the quadratic terms: $(\bar{w}_s, \bar{v}_s) = (\sqrt{-r/\gamma}, 0)$ and $(\bar{w}_s, \bar{v}_s) = \{\sqrt{\sigma/2\gamma}, \pm [(2r + \sigma)/2\gamma]^{1/2}\}$. The $\bar{v}_s = 0$ solution is stable for $\gamma > 0$ ($r = -1$) and unstable for $\gamma < 0$ ($r = 1$), whereas the $\bar{v}_s \neq 0$ solution is always unstable.

Figure 7(a) shows a simulation of the original field

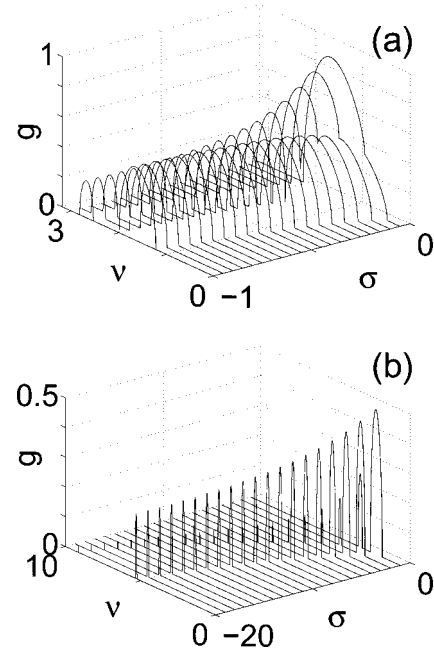


Fig. 6. Gain profiles of the $r = -1$ solutions for $\tilde{\gamma} = 0$.

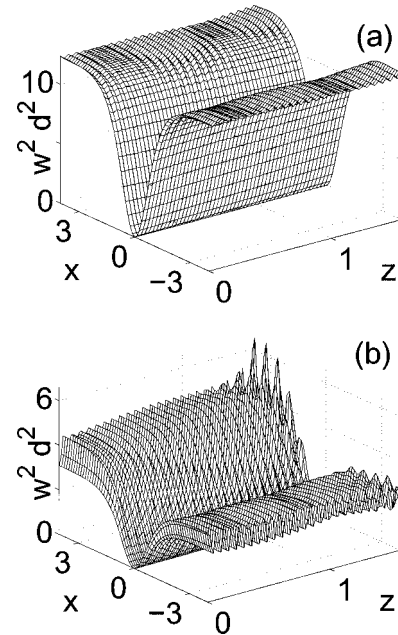


Fig. 7. Evolution of the fundamental intensity w , corresponding to the solutions (a) Eq. (11) with $\gamma = 0.08$ and (b) Eq. (12) with $\gamma = -0.08$. The gratings parameters are $d'_0/d' = 2.8$ and $a'/\kappa = 0.36$. $r = -1$.

equations (1) with an initial condition corresponding to the stable nonlinear Schrödinger soliton [Eq. (11)]. No visible shedding of radiation occurs, and the fundamental intensity contains only rapid, small oscillations superimposed upon the large average beam, which is typical for stable, bright QPM solitons.^{20,22} The soliton propagates stably beyond $z = 150$, which corresponds to 150 diffraction lengths or more than 2000 coherence lengths. Thus the soliton is stable according to any reasonable experimental definition. In contrast, simulations of the two-wave dark soliton [Eq. (12)] over short distances [Fig. 7(b)] confirm that it is indeed modulationally unstable. We note that a small modulation (of spatial frequency $\nu \approx 10$) finally develops in Fig. 7(a), which indicates a weak instability that is not picked up by the averaged-field equations.

4. EXACT PLANE-WAVE SOLUTIONS

The stability analysis with the averaged-field equations found regions of stability. But these regions possibly lie at or beyond the limits of validity of the first-order perturbation theory. Additionally, propagation simulations showed weak instabilities that were not predicted by the averaged theory. Clearly, a thorough investigation requires a more-exact technique that does not rely on the perturbation theory. Therefore we numerically find the exact plane-wave solutions and apply an exact Floquet analysis^{15,37} to determine their stability. We begin with Eqs. (2), substituting into it Fourier expansions (3) and (4). This gives a set of coupled equations for the plane-wave coefficients w_n and v_n :

$$\begin{aligned} -(n\kappa + r)w_n + \sum_{l,p} D_{n+l-p-1}w_l^*v_p &= 0, \\ -(n\kappa + \sigma)v_n + a' \sum_l g_{n-l}v_l \\ &+ \sum_{l,p} D_{n-l-p+1}w_l w_p = 0, \end{aligned} \quad (13)$$

where $D_n = d'g_n + d'_0\delta_{n,0}$. We may rewrite these equations more succinctly as $\mathbf{F}_n = 0$.

We find the solution to Eqs. (13) numerically, using a relaxation technique based on Newton's method. An initial guess of the components w_n and v_n [which we represent by the vector $\mathbf{u}^{(0)}$], calculated from the approximate first-order solutions, is iteratively corrected by the increment $\Delta\mathbf{u}^{(k+1)} = -\mathbf{J}^{-1}(\mathbf{u}^{(k)})\mathbf{F}(\mathbf{u}^{(k)})$, where the Jacobean matrix is

$$\{\mathbf{J}\}_{l,q} = \begin{bmatrix} \frac{\partial F_l}{\partial w_q} & \frac{\partial F_l}{\partial v_q} & \frac{\partial F_l}{\partial w_q^*} & \frac{\partial F_l}{\partial v_q^*} \\ \frac{\partial F_l^*}{\partial w_q} & \frac{\partial F_l^*}{\partial v_q} & \frac{\partial F_l^*}{\partial w_q^*} & \frac{\partial F_l^*}{\partial v_q^*} \end{bmatrix}. \quad (14)$$

Figure 8 shows some of the exact solutions for $r = -1$ when both a linear and a nonlinear grating are present, with parameters $a'/\kappa = 0.158$, $d'_0/d' = 5/3$, and $\eta = 1$. These gratings correspond to the GaAs/GaAlAs structure reported in Ref. 28. Figure 8(a) shows the ratio

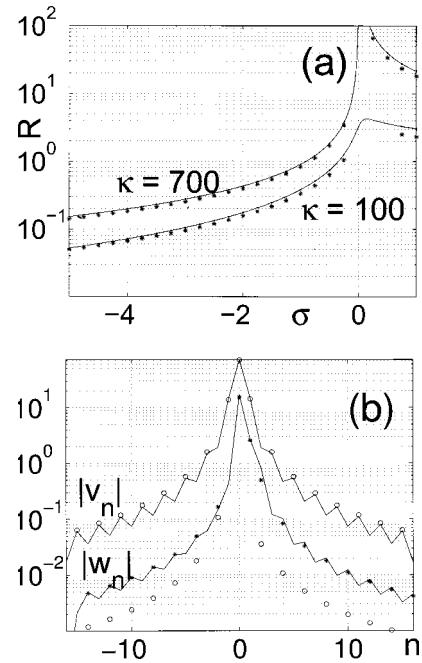


Fig. 8. (a) Ratio $R = |v_0|^2/|w_0|^2$ versus mismatch parameter σ calculated exactly (asterisks) and by the averaged-field theory (solid curves). (b) Fourier components of the solution for $\kappa = 700$, $\sigma = 1$ calculated exactly (solid curves) and by the averaged-field theory (asterisks for w_n and circles for v_n). $r = -1$.

$R = |v_0|^2/|w_0|^2$ versus mismatch parameter σ for grating wave numbers $\kappa = 700$ and $\kappa = 100$. These values of κ give $\tilde{\gamma} < 0.1$, which means that these solutions lie outside the stability region predicted by the average theory (Fig. 4). Not shown are the solutions at $\sigma = 0$ for which \bar{w} is zero or negligibly small. As the figures show, in terms of the dc intensity ratio the exact solutions consistently agree well with the approximate solutions found by averaging.

Figure 8(b) gives the Fourier coefficients $|w_n|$ and $|v_n|$ for a representative solution. Even though the amplitudes do not decrease exponentially with n , the decrease is sufficiently rapid that the tenth component is almost 3 orders of magnitude less than the dc value. Thus in our calculations we typically include as many as $n = \pm 16$ components in the Fourier expansions.

That the approximate theory accurately predicts the averaged properties of the system is well known. However, Fig. 8(b) shows that this approach does not properly account for the higher-order Fourier components (particularly the odd components of w and the even components of v), which are important for a correct MI analysis.

5. EXACT STABILITY ANALYSIS

A. Floquet Theory

We determine the linear stability of the plane-wave solutions (w_s, v_s) by using exact Floquet theory.¹⁵ For perturbations of transverse frequency offset ν ,

$$w(x, z) = w_s(z) + \delta_1(z)\exp(-i\nu x) + \delta_2^*(z)\exp(i\nu x),$$

$$v(x, z) = v_s(z) + \delta_3(z)\exp(-i\nu x) + \delta_4^*(z)\exp(i\nu x), \quad (15)$$

the linear evolution is governed by the linearized equation $\partial_z \mathbf{P} = M(z)\mathbf{P}$, where

$$\mathbf{P} = \begin{pmatrix} \delta_1 \\ \delta_2 \\ \delta_3 \\ \delta_4 \end{pmatrix}, \quad M = i \begin{pmatrix} a & b & c^* & 0 \\ -b^* & -a & 0 & -c \\ 2c & 0 & d & 0 \\ 0 & -2c^* & 0 & -d \end{pmatrix}, \quad (16)$$

with $a = -\nu^2/2 - r$, $b = v_s(z)\chi(z)\exp(i\kappa z)$, $c = w_s(z)\chi(z)\exp(-i\kappa z)$, and $d = -\nu^2/4 - \sigma + \alpha'(z)$. Because of the periodicity in the coefficients α' and χ' and in the solutions w_s and v_s , matrix M , which governs the growth of linear perturbations, is also periodic, with period $z_p = 2\pi/|\kappa|$. To determine the stability, we need only find the eigenvalues λ_i of the mapping δT of the solution over one period¹⁵: $\mathbf{P}(z + z_p) = \delta T\mathbf{P}(z)$.

Now, for $\{\mathbf{P}(z)\}_i = \delta_{i,k}$ for some $k \in \{1, 2, 3, 4\}$, the solution one period later, $\mathbf{P}(z + z_p)$, will be the k th column of δT . Thus we may construct constant matrix δT by integrating linearized equation $\partial_z \mathbf{P} = M(z)\mathbf{P}$ out to $z = z_0 + z_p$ for the four initial conditions $\{\mathbf{P}(z_0)\}_i = \delta_{i,k}$ that correspond to each $k \in \{1, 2, 3, 4\}$. This is done numerically by the fourth-order Runge-Kutta method. If all the λ_i lie on the unit circle for every ν , then the solutions w_s and v_s are stable; otherwise there is a net gain whose profile is well estimated by the maximum eigenvalue growth rate $g = \max\{\Re[\ln(\lambda_i)/z_p]\}$.

B. Applications I: Efficient Phase Matching

To help in the analysis of the Floquet results, we divide the situations into two regimes: efficient phase matching, in which the residual effective mismatch is much smaller than the material mismatch ($\tilde{\beta}' \ll \beta'$), and poor phase matching. In the former case, the averaged-field theory is expected to hold, whereas in the latter the large residual mismatch invalidates the assumptions made in the perturbation theory (i.e., $\tilde{\beta}' \ll \kappa$).

We consider first the case that corresponds to having no effective quadratic nonlinearity in the averaged-field analysis (i.e., $\rho = 0$), to see whether the Floquet analysis confirms the strong prediction of the averaged-field theory that the solutions and their MI properties will be governed by cubic nonlinearities.

To make the comparison with the exact Floquet analysis, consider a physical system with the parameters $a'/\kappa = 5/14$ and $d'_0/d' = 14/5$, for which $\rho = 0$. Figure 9(a) shows the MI gain profiles (gain versus the spatial frequency ν of the perturbation) for the $\bar{v}_s \neq 0$ solution, which corresponds to the unstable background in Fig. 7(b), calculated by both the exact Floquet theory (solid curves) and the averaged-field theory (dashed curve). The Floquet theory predicts that each of the two solutions will have its own distinct gain curve, whereas in the approximate calculation the two solutions ($\pm\bar{v}$) give the same degenerate gain curve. The approximate and exact results agree well away from $\nu = 0$ but differ noticeably near $\nu = 0$. For comparison, Fig. 9(b) plots the gain

curve for $|\rho| = 2/(15\pi)$, with $a'/\kappa = 1/3$. Here the Floquet curves for the two solutions differ more markedly, but each agrees well with its approximate counterpart, which now corresponds to points on the (U2) and (G) branches in Fig. 2. The discrepancy in Fig. 9(a) is due to the presence of higher-order terms that have been neglected in the averaged theory and that break the degeneracy of the nonlinear Schrödinger solution [Eq. (12)]. These terms, of order ϵ^2 and higher, would need to be included for a consistent theory that accurately predicts the gain when ν is smaller than order ϵ^1 , especially when the quadratic (order ϵ^0) nonlinearity is absent.

The $\bar{v}_s = 0$ solution is predicted by the averaged-field theory to be stable. However, the exact Floquet theory shows that there is some nonzero gain at high spatial frequencies. But the gain curves are extremely narrow and have low peak values: The largest region of gain at $\nu = 9.9$ is only $\Delta\nu = 0.05$ wide, with a maximum of $g = 0.21$, which corresponds to the weak instability of the simulation in Fig. 7(a).

A Floquet analysis of the solutions shown in Fig. 8 does not find any points that are stable. This result is not surprising, because these points lie outside the stability region predicted by the first-order analysis. But exact solutions that correspond to the stable lowest branch of averaged solutions can be found for lower values of $|\kappa|$, the grating wave number. A plot of the maximum MI gain [Fig. 10(a)], however, shows that these solutions exhibit a weak, but nonzero, MI gain. This residual gain ($\approx 0.2 \rightarrow 1$) increases for decreasing κ and is caused by the narrow gain bands that are once again present at high ν . Other simulations confirm that such high- ν peaks, which are not predicted by the averaged theory, are a general feature of the gain spectrum for efficient QPM gratings.

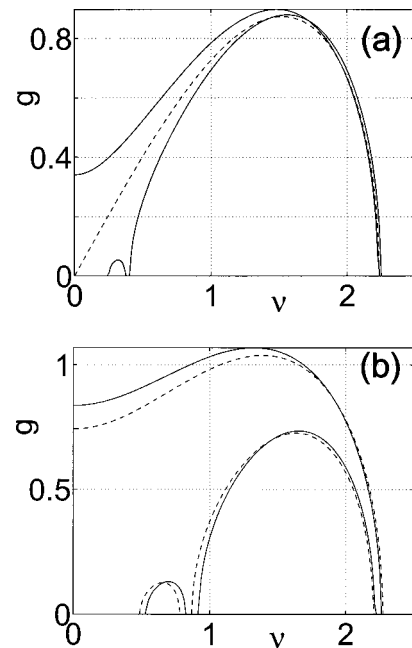


Fig. 9. Gain curves for the dual plane-wave solution when (a) $\rho = 0$ and (b) $|\rho| = 2/(15\pi)$, for $\gamma < 0$ and $\sigma = -0.5$ ($\tilde{\beta}' = -3/2$). Dashed curves, averaged-field results; solid curves, exact Floquet results.

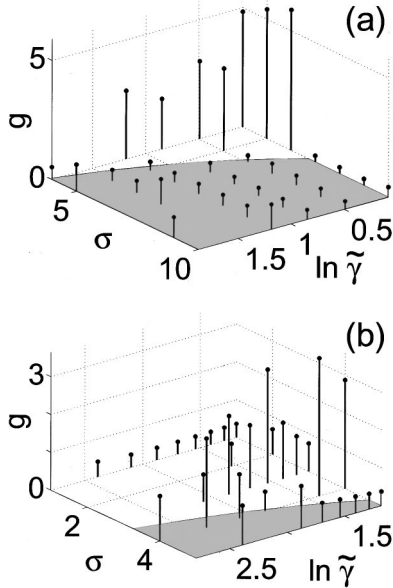


Fig. 10. Maximum gain for solutions with (a) $5 \leq \kappa \leq 30$ and (b) $1 < \kappa < 10$. The regions of zero gain predicted from the averaged-field theory are shaded. $d'_0/d' = 5/3$ and $a'/\kappa = 0.316$.

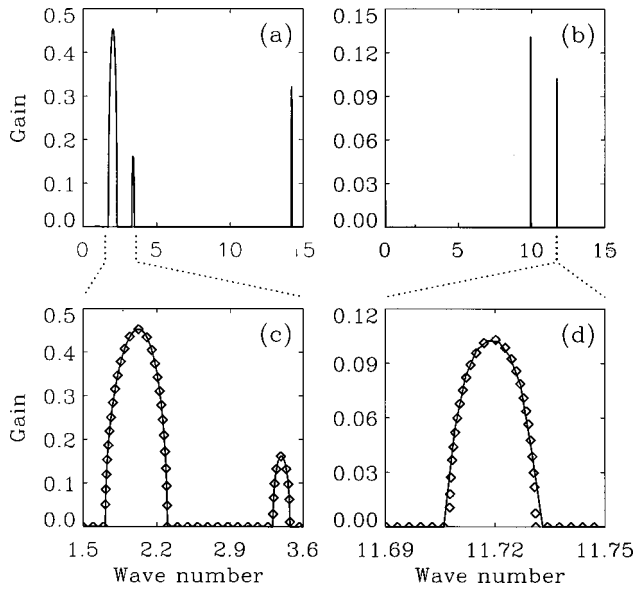


Fig. 11. Floquet gain spectra for (a) the LiNbO₃ and (b) the GaAs/AlAs gratings, for $\sigma = -2$. The diamonds show the averaged-field results in (c) and the equivalent non-phase-matched homogeneous results in (d).

To analyze the MI spectrum in detail and illustrate the physical origin of these high- ν peaks, we consider the spectra of two concrete examples that are typical for efficiently phase-matched gratings ($|\tilde{\beta}| \ll |\beta|$). Figure 11(a) is the spectrum for a conventional domain-reversal grating in LiNbO₃ ($a' = d'_0 = 0$) for $r = -1$, $\kappa = 100$, and exact phase matching ($\sigma = -2$), and Fig. 11(b) is that of a GaAs/AlAs superstructure with a nonlinear grating etched through quantum-well disordering.³⁸ ($d'_0/d' = 4.6$) and a linear grating chosen to be $a'/\kappa = 10/46$. The former example is unstable according to the averaged-field analysis and possesses a low- ν gain that is

accurately predicted by the average theory [Fig. 11(c)]; the latter example lies in the predicted stable region and thus has no gain at low ν .

The high- ν gain bands are related to the inherent MI in the non-phase-matched, homogeneous $\chi^{(2)}$ material (i.e., with no grating), as demonstrated by the close match between the homogeneous gain band [Fig. 11(d)] and one of the peaks in Fig. 11(b). Each gain peak that appears in the homogeneous spectrum usually also appears in the Floquet spectrum, typically with the same height and spectral location. Often, as in Fig. 11(b), the homogeneous peak is split into several closely spaced secondary peaks by the grating. Sometimes, as for a symmetric grating ($d'_0 = 0$) such as in LiNbO₃ [Fig. 11(a)], the original homogeneous peak is suppressed, leaving only the secondary peaks in the high- ν part of the spectrum.

C. Applications II: Poor Phase Matching

As we saw in Subsection 3.B, attempting to reach the stable branch of the approximate solutions while maintaining a large quadratic nonlinearity (ρ) usually involves the poor-phase-matching regime, where the averaged theory no longer holds. To illustrate what happens, we show in Fig. 10(b) the maximum growth rate of instabilities for the grating $d'_0/d' = 5/3$ and $a'/\kappa = 0.316$. Here $-\tilde{\beta}' > 3$ is rather large and $\kappa < 10$ is fairly small, so the first-order perturbation results are not guaranteed to be valid in this region. That the Floquet theory found solutions with large gain in the predicted stable region is therefore not surprising.

The differences between the averaged and the exact treatments for these parameters are further illustrated by a comparison of the gain profiles, which we make in Fig. 12 for two representative points. The averaged so-

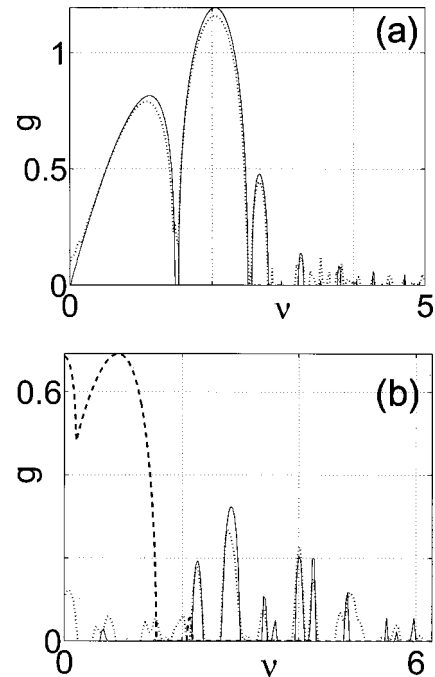


Fig. 12. Gain curves for (a) $\kappa = 2$ and $\sigma = 4$ and (b) $\kappa = 6$ and $\sigma = 1$, calculated from Floquet theory (solid curves) and simulations (dotted curves). The averaged theory predicts a stable solution in (a) and a gain marked by the dashed curve in (b). $d'_0/d' = 5/3$ and $a'/\kappa = 0.316$.

lution that corresponds to Fig. 12(a) ($\kappa = 2, \sigma = 4$) lies in the predicted stable region, but the Floquet analysis gives a nonzero gain that is large and broadband. The exact gain curve in Fig. 12(b) ($\kappa = 6, \sigma = 1$) consists of a number of narrow peaks distributed over a range of frequencies, whereas first-order analysis predicts a larger, broadband curve that lies at low frequencies.

In Subsection 5.B we saw that, where the grating efficiently phase matches the fields, the MI gain spectrum falls into two well-separated parts: the low-frequency bands induced by the periodicity and accurately predicted by the averaged equations, and the high-frequency bands related to inherent $\chi^{(2)}$ gain. When residual mismatch $|\tilde{\beta}|$ is larger than (and not so different from) $|\beta|$, we find that the two regions no longer are well separated and that the averaged equations no longer accurately predict the low- ν bands. For very poor phase matching, as in this subsection, the two features mix, producing a complicated gain spectrum [e.g., Fig. 12(b)] that cannot be simply related to the distinct underlying physical mechanisms.

D. Experimental Stability

In all our results we found no solutions that, mathematically speaking, were modulationally stable. Even in the region where the averaged-field analysis predicts stability, there is a residual gain that corresponds to the high- ν bands. However, this residual gain is not large ($g \leq 0.3$ or smaller for material mismatch $|\beta'| \sim 10$ or larger) and may be neglected under a reasonable definition of experimental stability. If perturbations do not increase by any orders of magnitude within a few diffractions lengths, which is a typical experimental length scale, then the instability will not be detectable. However, if we do neglect these high- ν bands, such that the averaged and Floquet results coincide, then we must also allow some solutions that were previously classed as unstable by the averaged-field analysis to be classed as stable, because the low- ν bands are sometimes smaller than the high- ν bands. These additional solutions correspond to the light-gray regions in Fig. 5 for $r = -1$ as well as similar regions for $r = 0$ and $r = 1$, which were previously regarded as totally unstable branches.

6. PROPAGATIVE SIMULATIONS

To confirm the Floquet predictions of the MI spectra, we perform numerical simulations of (scaled) field equations (2). We can determine gain curves by launching plane waves seeded with small fluctuations, which then evolve linearly. Using Gaussian white noise to excite all frequencies, we calculate the gain curve from the Fourier transformed amplitude³⁶ \tilde{E}_1 as $\bar{g}(\nu) = [\ln |E_1(Z_2, Y)| - \ln |\tilde{E}_1(Z_1, Y)|] / (Z_2 - Z_1)$, where $Y = \sqrt{\eta\nu}$.

Propagation calculations confirm, for example, the gain curves predicted by Floquet theory in Fig. 9(a). Importantly, they agree with the Floquet curves in regions where the averaged-field and Floquet theories predict different results, such as near $\nu = 0$ in these figures. A more dramatic illustration of this confirmation is shown in Fig. 12, where the averaged and exact predictions disagree markedly. Small, narrow peaks are difficult to dis-

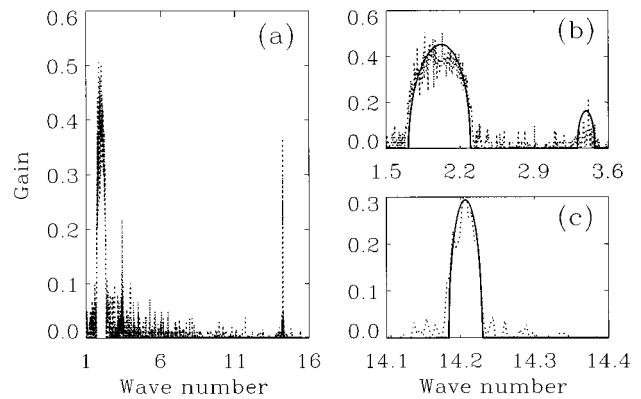


Fig. 13. (a) Gain profile calculated from propagative simulations for the same parameters as in Fig. 11(a). Comparisons with the Floquet theory (solid curves) are given in (b) and (c).

tinguish from the noise floor in these simulations, but the peaks seen in the smoothed data in Fig. 12(b) (dotted curves) clearly correspond to the largest Floquet peaks (solid curves). For the same reason, the small, narrow, high- ν bands predicted by Floquet theory are difficult to detect, but with a careful choice of simulation parameters these peaks can be seen, as shown in Fig. 13 for the LiNbO₃ grating. Clearly, the simulations confirm the Floquet calculations in both the low- ν [Fig. 13(b)] and the high- ν [Fig. 13(c)] regions.

7. CONCLUSIONS

In summary, we have determined the exact structure and modulational stability of plane-wave solutions in periodic $\chi^{(2)}$ materials, using both Floquet transfer-matrix calculations and direct numerical simulations. In particular, we found Fourier expansions of the plane waves in the propagation direction and used them in calculations of the gain spectrum (growth rate versus transverse frequency of the instability). We found that in the regime of efficient phase matching, because of the periodicity, the spectra contain gain bands both at low spatial frequency, which are caused by the phase-matching gratings, and at high spatial frequency, which are related to the inherent gain of homogeneous $\chi^{(2)}$ materials. For poor phase matching, the gain bands do not fall into these different regions of the spectrum and so cannot be attributed to specific underlying causes.

In the regime of efficient phase matching, the exact calculations were supplemented by a simpler averaged-field approach characterized by effective quadratic and induced cubic nonlinearities. For sufficiently large cubic nonlinearities and away from exact phase matching, the averaged-field theory predicts stability for some solutions. However, the exact techniques showed that, whereas the averaged-field approach accurately predicts slowly varying properties of the system, it sometimes inaccurately treats the higher Fourier components, as these are treated to a lower order in the theory. It also shows inaccuracies in the MI predictions; it is unable to predict the high-frequency gain bands. Nevertheless, the averaged-field theory accurately describes low-frequency gain, even in the extreme case in which the effective quadratic nonlinearity is canceled by competition between

the linear and the nonlinear gratings. Furthermore, because the high-frequency gain is often small, the averaged-theory zero-gain predictions can be accurate under experimentally relevant definitions of stability.

ACKNOWLEDGMENT

This research was supported by the Danish Technical Research Council under grant 26-00-0355.

J. F. Corney's email address is jfc@imm.dtu.dk.

REFERENCES

- G. I. Stegeman, D. J. Hagan, and L. Torner, " $\chi^{(2)}$ cascading phenomena and their applications to all-optical signal processing, mode-locking, pulse compression and solitons," *Opt. Quantum Electron.* **28**, 1691–1740 (1996).
- K. Hayata and M. Koshiba, "Multidimensional solitons in quadratic nonlinear media," *Phys. Rev. Lett.* **71**, 3275–3278 (1993).
- L. Torner, C. R. Menyuk, W. E. Torruellas, and G. I. Stegeman, "Two-dimensional solitons with second-order nonlinearities," *Opt. Lett.* **20**, 13–15 (1995).
- L. Bergé, V. K. Mezentsev, J. J. Rasmussen, and J. Wyller, "Formation of stable solitons in quadratic nonlinear media," *Phys. Rev. A* **52**, R28–R31 (1995).
- D. E. Pelinovsky, A. V. Buryak, and Y. S. Kivshar, "Instability of solitons governed by quadratic nonlinearities," *Phys. Rev. Lett.* **75**, 591–595 (1995).
- B. A. Malomed, P. D. Drummond, H. He, A. Berntson, D. Anderson, and M. Lisak, "Spatiotemporal solitons in multidimensional optical media with a quadratic nonlinearity," *Phys. Rev. E* **56**, 4725–4735 (1997).
- R. Schiek, Y. Baek, and G. I. Stegeman, "One-dimensional spatial solitary waves due to cascaded second-order nonlinearities in planar waveguides," *Phys. Rev. E* **53**, 1138–1141 (1996).
- W. E. Torruellas, Z. Wang, D. J. Hagan, E. W. Van Stryland, G. I. Stegeman, L. Torner, and C. R. Menyuk, "Observation of two-dimensional spatial solitary waves in a quadratic medium," *Phys. Rev. Lett.* **74**, 5036–5039 (1995).
- X. Liu, K. Beckwitt, and F. Wise, "Two-dimensional optical spatiotemporal solitons in quadratic media," *Phys. Rev. E* **62**, 1328–1340 (2000).
- E. Lopez Lago, V. Couderc, C. de Angelis, F. Gringoli, and A. Barthélémy, "Experimental demonstration of the self-trapping of a weak probe induced by a quadratic spatial soliton," in *Nonlinear Guided Waves and Their Applications*, Vol. 55 of OSA Trends in Optics and Photonics Series (Optical Society of America, Washington, D.C., 2001), pp. 379–381.
- V. Couderc, E. Lopez Lago, C. Simos, and A. Barthélémy, "Experiments in quadratic spatial soliton generation and steering in a noncollinear geometry," *Opt. Lett.* **26**, 905–907 (2001).
- W. E. Torruellas, G. Assanto, B. L. Lawrence, R. A. Fuerst, and G. I. Stegeman, "All-optical switching by spatial walkoff compensation and solitary-wave locking," *Appl. Phys. Lett.* **68**, 1449–1451 (1996).
- P. Di Trapani, W. Chinaglia, S. Minardi, A. Piskarskas, and G. Valiulis, "Observation of quadratic optical vortex solitons," *Phys. Rev. Lett.* **84**, 3843–3846 (2000).
- S. Trillo and P. Ferro, "Modulational instability in second-harmonic generation," *Opt. Lett.* **20**, 438–440 (1995).
- R. A. Fuerst, D.-M. Baboiu, B. Lawrence, W. E. Torruellas, G. I. Stegeman, S. Trillo, and S. Wabnitz, "Spatial modulational instability and multisolitonlike generation in a quadratically nonlinear optical medium," *Phys. Rev. Lett.* **78**, 2756–2759 (1997).
- H. Fang, R. Malendevich, R. Schiek, and G. I. Stegeman, "Spatial modulational instability in one-dimensional lithium niobate slab waveguides," *Opt. Lett.* **25**, 1786–1788 (2000).
- R. Schiek, H. Fang, R. Malendevich, and G. I. Stegeman, "Measurement of modulational instability gain of second-order nonlinear optical eigenmodes in a one-dimensional system," *Phys. Rev. Lett.* **86**, 4528–4531 (2001).
- O. Bang, Y. S. Kivshar, and A. Buryak, "Bright spatial solitons in defocusing Kerr media supported by cascaded nonlinearities," *Opt. Lett.* **22**, 1680–1682 (1997).
- T. J. Alexander, A. V. Buryak, and Y. S. Kivshar, "Stabilization of dark and vortex parametric spatial solitons," *Opt. Lett.* **23**, 670–672 (1998).
- C. B. Clausen, O. Bang, and Y. S. Kivshar, "Spatial solitons and induced Kerr effects in quasi-phase-matched quadratic media," *Phys. Rev. Lett.* **78**, 4749–4752 (1997).
- O. Bang, C. B. Clausen, P. L. Christiansen, and L. Torner, "Engineering competing nonlinearities," *Opt. Lett.* **24**, 1413–1415 (1999).
- J. F. Corney and O. Bang, "Solitons in quadratic nonlinear photonic crystals," *Phys. Rev. E* **64**, 047601 (2001).
- P. Di Trapani, A. Bramati, S. Minardi, W. Chinaglia, C. Conti, S. Trillo, J. Kilius, and G. Valiulis, "Focusing versus defocusing nonlinearities due to parametric wave mixing," *Phys. Rev. Lett.* **87**, 183902 (2001).
- M. M. Fejer, G. A. Magel, D. H. Jundt, and R. L. Byer, "Quasi-phase-matched second harmonic generation: tuning and tolerances," *IEEE J. Quantum Electron.* **28**, 2631–2654 (1992).
- T. Suhara and H. Nishihara, "Theoretical analysis of waveguide second-harmonic generation phase matched with uniform and chirped gratings," *IEEE J. Quantum Electron.* **26**, 1265–1276 (1990).
- B. Jaskorzynska, G. Arvidsson, and F. Laurell, "Periodic structures for phase-matching in second harmonic generation in titanium lithium niobate waveguides," in *Integrated Optical Circuit Engineering III*, R. Th. Kersten, ed., Proc. SPIE **651**, 221–228 (1986).
- C. L. Tang and P. P. Bey, "Phase matching in second-harmonic generation using artificial periodic structure," *IEEE J. Quantum Electron.* **9**, 9–17 (1973).
- D. V. Petrov, "Nonlinear phase shift by cascaded quasi-phase-matched second harmonic generation," *Opt. Commun.* **131**, 102–106 (1996).
- J. F. Corney and O. Bang, "Modulational instability in periodic quadratic nonlinear materials," *Phys. Rev. Lett.* **87**, 133901 (2001).
- A. Kobayakov, F. Lederer, O. Bang, and Y. S. Kivshar, "Nonlinear phase shift and all-optical switching in quasi-phase-matched quadratic media," *Opt. Lett.* **23**, 506–508 (1998).
- O. Bang, T. W. Graversen, and J. F. Corney, "Accurate switching intensities and length scales in quasi-phase-matched materials," *Opt. Lett.* **26**, 1007–1009 (2001).
- J. A. Armstrong, N. Bloembergen, J. Ducuing, and P. S. Pershan, "Interactions between light waves in a nonlinear dielectric," *Phys. Rev.* **127**, 1918–1939 (1962).
- C. R. Menyuk, R. Schiek, and L. Torner, "Solitary waves due to $\chi^{(2)}$: $\chi^{(2)}$ cascading," *J. Opt. Soc. Am. B* **11**, 2434–2443 (1994).
- O. Bang, "Dynamical equations for wave packets in material with both quadratic and cubic response," *J. Opt. Soc. Am. B* **14**, 51–61 (1997).
- H. He, P. D. Drummond, and B. A. Malomed, "Modulational stability in dispersive optical systems with cascaded nonlinearity," *Opt. Commun.* **123**, 394–402 (1996).
- H. He, A. Arraf, C. M. de Sterke, P. D. Drummond, and B. A. Malomed, "Theory of modulational instability in Bragg gratings with quadratic nonlinearity," *Phys. Rev. E* **59**, 6064–6078 (1996).
- T. Cretegnny, T. Dauxois, S. Ruffo, and A. Torcini, "Localization and equipartition of energy in the β -FPU chain: chaotic breathers," *Physica D* **121**, 109–126 (1998).
- A. Saher Helmy, D. C. Hutchings, T. C. Kleckner, J. H. Marsh, A. C. Bryce, J. M. Arnold, C. R. Stanley, J. S. Aitchison, C. T. A. Brown, K. Moutzouris, and M. Ebrahimzadeh, "Quasi phase matching in GaAs-AlAs superlattice waveguides through bandgap tuning by use of quantum-well intermixing," *Opt. Lett.* **25**, 1370–1372 (2000).